# Influence of magnetic angle on the E × B drift in a magnetic presheath

Cite as: Phys. Plasmas **28**, 083507 (2021); https://doi.org/10.1063/5.0046708 Submitted: 05 February 2021 . Accepted: 23 July 2021 . Published Online: 09 August 2021









## ARTICLES YOU MAY BE INTERESTED IN

Turbulence transport in the solar corona: Theory, modeling, and Parker Solar Probe Physics of Plasmas 28, 080501 (2021); https://doi.org/10.1063/5.0055692

Characterization of injection and confinement improvement through impurity induced profile modifications on the Wendelstein 7-X stellarator

Physics of Plasmas 28, 082506 (2021); https://doi.org/10.1063/5.0047274

Kinetic simulation of electron cyclotron resonance assisted gas breakdown in split-biased waveguides for ITER collective Thomson scattering diagnostic

Physics of Plasmas 28, 082505 (2021); https://doi.org/10.1063/5.0055461





# Influence of magnetic angle on the E $\times$ B drift in a magnetic presheath

Cite as: Phys. Plasmas 28, 083507 (2021); doi: 10.1063/5.0046708

Submitted: 5 February 2021 · Accepted: 23 July 2021 ·

Published Online: 9 August 2021









#### **AFFILIATIONS**

Department of Physics and Astronomy and Center for KINETIC Plasma Physics, West Virginia University, Morgantown, West Virginia 26506, USA

<sup>a)</sup>Author to whom correspondence should be addressed: ddc0008@mix.wvu.edu

### **ABSTRACT**

In this work, we provide experimental measurements of the  $E \times B$  flow above a non-magnetic, absorbing boundary in a magnetized plasma. Measurements are taken as a function of the angle between the background magnetic field and the boundary normal. The measurements are compared to computational predictions for oblique magnetic fields based on Chodura's model. Ion flow measurements were obtained with laser induced fluorescence and the presheath potential structure was measured with an emissive probe. The ions were found to accelerate to nearly 30% of the sound speed parallel to the boundary at oblique angles of the magnetic field ( $\sim 80^{\circ}$ ) and the ion speed at the electrostatic sheath edge was found to decrease with angle. The edge of the magnetic presheath has been experimentally determined based on the appearance of the  $\mathbf{E} \times \mathbf{B}$  drift and is found to be independent of the angle of the magnetic field. We also demonstrate that laser induced fluorescence is suitable as a non-perturbative diagnostic to measure the electric field in a magnetized sheath.

Published under an exclusive license by AIP Publishing. https://doi.org/10.1063/5.0046708

# I. INTRODUCTION

Sheaths are an inescapable part of laboratory plasmas and create a region of complex dynamics near a boundary. This is necessary to balance the fluxes of ions, neutrals, and electrons from the plasma to the boundary surface. In standard theoretical analysis, a boundary in an unmagnetized plasma will produce two regions: the electrostatic sheath and a collisional presheath. When the plasma is magnetized, the complexity of collisional presheath increases significantly. Magnetic fields, unless they are perfectly parallel to the presheath's electric field, break the symmetry of this region by introducing motion in new directions. This symmetry break begins in the magnetic presheath, a region unique to magnetized plasmas (see Fig. 1). Therefore, ions falling through the magnetic presheath will experience additional

Magnetized sheath theory suggests that an ion, in the collisional presheath, will feel a weak electric field from the boundary that accelerates it parallel to the background magnetic field. These ions will reach speeds greater than or equal to the ion sound speed,  $c_s$ , at the entrance of the magnetic presheath. The magnetic presheath then redirects these ions from traveling at the sound speed along the magnetic field to traveling at the sound speed perpendicular to the boundary at the edge of the electrostatic sheath. The magnetic presheath is also subject to cross field flows since the background magnetic field couples with the electric field, created by the difference between the boundary and plasma potentials, and drives  $\mathbf{E} \times \mathbf{B}$  flows. Understanding the full range of ion motion in the presheath is necessary to accurately predict a wide range of plasma-material interactions.

Plasma-material interactions, particularly sputtering and erosion, play important roles in a variety of systems with oblique magnetic fields, such as the divertor region in magnetic fusion devices. In tokamaks, impurities released by ion bombardment cause changes in the plasma properties above the divertors and are an important factor in achieving detached divertors.<sup>2</sup> Flows in the plasma edge, specifically diamagnetic drifts and the  $\mathbf{E} \times \mathbf{B}$  drift produced by the divertor,<sup>3</sup> can compound to significantly affect edge turbulence, retention rates, and the threshold for a detached divertor. 4-6 Cross field flows also affect divertor recycling, an effect that cannot fully be explained by classical sheath conditions.<sup>7</sup> Recombination in tokamaks is often neglected in collisional models, but near the divertor recombination can play an important role in balancing particle flux.8 Therefore, the flow of ions in a magnetized sheath with oblique magnetic fields is an important consideration for models of ion dynamics in the plasma edge.

Since the first magnetized presheath model in 1982, there have been many theoretical advances. Full 3D effects and collisions have been included11,12 as well as more precise electric potential modeling. 13,14 However, these advanced models have identified new issues to

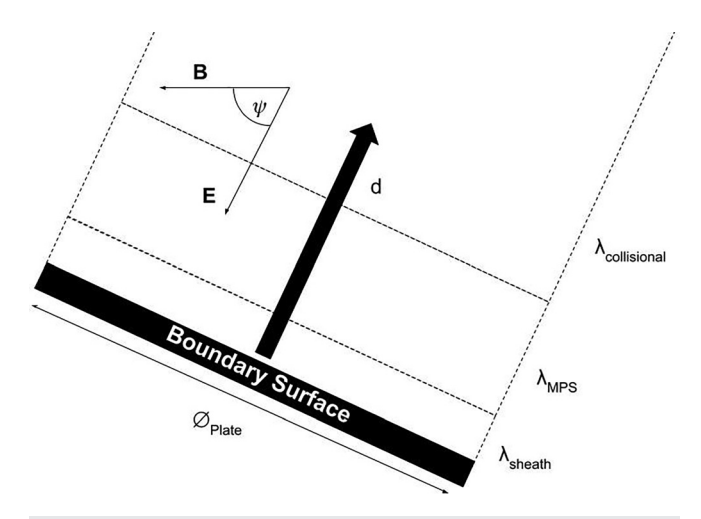


**FIG. 1.** Diagram of the sheath and presheath structures in a magnetized plasma. The angle between the boundary's electric field and background magnetic field is  $\psi$ , the normal distance is given by d,  $\oslash_{\textit{Plate}}$  is the diameter of the plate (76.2 mm). The three regions for a magnetized plasmas are shown: the electrostatic sheath  $(\lambda_{\textit{sheath}})$ , the magnetic presheath  $(\lambda_{\textit{MPS}})$ , and the collisional presheath  $(\lambda_{\textit{collisional}})$ .

be addressed, such as complicated space-charge effects, <sup>15,16</sup> infinite potentials, <sup>17</sup> and a need to redefine regime boundary locations. <sup>18</sup> Additionally, to capture individual particle motion and turbulent effects, the new models need to be gyrokinetic rather than fluid, increasing the computation cost of understanding magnetized sheaths, <sup>9,19</sup>

Experiment has lagged behind both theory and numerical studies with regard to the magnetic presheath. Most of the experimental investigations into the ion and neutral populations of the magnetic presheath are relatively recent. Using laser induced fluorescence (LIF), those experiments were able to study critical collisional processes and ion flows in magnetized sheaths for a range of collisional conditions. For specific angles between the magnetic and electric field, relative to the plasma boundary, results have shown quantitative agreements between experiment and computation when ion-neutral collisional effects were taken into account. The aim of this work is to provide measurements of the  $\mathbf{E} \times \mathbf{B}$  flow in a magnetized sheath over a range of plate angles against which future computational studies may be benchmarked.

The angle between the boundary normal and the background field is referred to here as  $\psi$ . Chodura's equation predicts the length of the magnetic presheath,  $\lambda_{mps}$ , which starts at the edge of the electrostatic sheath and extends into the bulk plasma a distance

$$\lambda_{mps} = \sqrt{6} \frac{c_s}{\omega_{ci}} \sin \psi. \tag{1}$$

In Eq. (1),  $\omega_{ci}$  is the ion cyclotron frequency and  $c_s$  is the ion sound speed given by

$$c_s = \sqrt{\frac{k_B T_e}{m_i}}. (2)$$

Here,  $k_B$  is the Boltzmann constant,  $T_e$  is the electron temperature, and  $m_i$  is the ion mass.

In this work, we measure the  $\mathbf{E} \times \mathbf{B}$  drift, parallel to the boundary, as a function of distance normal to the boundary for different angles of incident background magnetic field. We also present measurements of ion temperature, bulk ion flow, and plasma potential,  $T_{\eta},\ U_{\eta},$  and  $V_p$ , respectively, where  $\eta$  denotes the direction of the measurement. Measurements are performed in the magnetic presheath for a high density  $(n_i \approx 3.0 \times 10^{17}~\text{m}^{-3})$  argon plasma above a conductive, unmagnetized, grounded surface. The measurements are performed at distances  $\leq 36~\text{mm}$  from the boundary surface. This range should encompass the entire magnetic presheath and the beginning of the collisional regime. We cannot resolve the electrostatic sheath because the Debye length is  $\approx 0.03~\text{mm}$ , smaller than the spatial localization of our diagnostics. In keeping with previous experimental reports and computational studies, distance values are given in normalized units.  $^{11,18-20}$ 

The  $\mathbf{E} \times \mathbf{B}$  drift in the magnetized sheath is expected to be angle dependent and described simply by

$$\mathbf{v}_{\mathbf{E} \times \mathbf{B}} = \frac{E}{R} \sin \psi, \tag{3}$$

where B is the magnitude of the magnetic field and E is the magnitude of the presheath electric field, which is aligned anti-parallel with the boundary normal. Other, more nuanced descriptions of the drift have been used in simulations, but require additional measurements outside the scope of this work. 13 Since the magnetic field strength is held constant, the drift speed is expected to depend on the angle  $\psi$  and E. The magnitude of the electric potential is predicted to increase with increasing  $\psi$ . As a function of distance from the boundary, the potential is expected to exhibit a sharp increase near the electrostatic sheath followed by a more gradual slower increase throughout the magnetic presheath. Therefore, changing the angle not only affects the value of  $\sin(\psi)$  but also *E*, both of which contribute to the drift. In this work, emissive probe measurements are used to calculate E from gradients in  $V_p$  and LIF provides measurements of the ion flows. The emissive probe provides for direct measurements of changes in the potential magnitude and structure as a function of  $\psi$ .

# II. EXPERIMENTAL APPARATUS A. HELIX facility

This work was conducted in the Hot hELIcon eXperiment (HELIX) at West Virginia University. HELIX's typical operating parameters produce electron temperatures of 3 - 10 eV and a max density of 10<sup>19</sup> m<sup>-3</sup>.<sup>21</sup> At these densities and temperatures, HELIX is well suited for studying fusion scrape-off layer dynamics. 19 The plasma chamber consists of a 19 cm long, m = +1 helicon antenna wrapped around a 61 cm long Pyrex tube with a 10 cm diameter. The antenna stage is mated to a 91 cm long,  $\oslash$  15 cm stainless steel chamber. 71 cm downstream from the center of the antenna are four ⊘ 6-in. crossing ports providing optical and probe access for this experiment. Gas is fed into the system through a mass flow controller upstream from the antenna. A steady-state, axial magnetic field is generated by ten electromagnets positioned along the length of the chamber and held fixed at 0.1 T. HELIX opens into an expansion chamber, which is beyond the experimental domain of the experiments reported here. The plasma is generated at 9.50 MHz by 650 W of steady-state rf power, supplied to the antenna through a  $\pi$ -matching network. The helicon source plasma has an intrinsic radius dependent, azimuthal flow.<sup>22</sup>

The background magnetic field is along the axis of the machine in the  $+\hat{z}$ -direction, resulting in an  $\mathbf{E} \times \mathbf{B}$  drift direction in  $-\hat{x}$ . For reference, see Fig. 2.

The boundary is a grounded ⊘ 76.2 mm disk placed in the core of the helicon plasma. Measurements were taken above the disk's center at distances d along its normal vector. The disk is constructed from 316 stainless steel with an integrated beam dump to minimize the reflection of injected light during LIF measurements. The beam dump is made from thin, non-magnetic stainless steel that was machined into razor blades. These were bound together and trap incident light so that it will not be reflected into the measurement region. Figure 2 shows the design of HELIX as well as the disk in the core of the helicon plasma along with the probe diagnostic. Magnetic field measurements confirm that the plate modifies the background field by  $\leq 1\%$ . To minimize variations in location for different angles of magnetic field incidence, the measurements were performed as close to the plate's pivot point as mechanically allowed. Therefore, the normal distances reported close to the boundary vary in spatial location by a maximum of 1 mm across angles for both laser and probe diagnostics. Care was taken to keep the plasma conditions constant, but for  $\psi = 60^{\circ}$  and  $\psi=45^\circ$  the system favored a new equilibrium in which the plasma core shifted 2 cm in the  $-\hat{x}$ -direction. Fiducial measurements obtained in the new equilibrium yielded ion flows and plasma potentials that were within error of those obtained for the other angles.

#### B. Laser induced fluorescence

LIF provides non-perturbative measurements of the ion velocity distribution function (IVDF) in the plasma. A laser is swept through an absorption transition of the target ion species while recording emission from the excited upper state of the transition. The absorption line is broadened by the Doppler shift from the thermally distributed ion velocities. The measured absorption line shape is converted into velocity space by

$$V = \frac{f - f_o}{f_o} c, \tag{4}$$

where f is the laser frequency in the lab frame,  $f_o$  is the frequency of the transition for the ion at rest, V is the velocity of the ion, and c is the speed of light in vacuum.

The Ar II transition used for these experiments begins with the  $3d^2G_{9/2}$  collisionally excited metastable state. This state can be produced from neutral gas, ions in other electronic states,<sup>23</sup> or stepwise excitation.<sup>24</sup> The metastable density is related to the LIF signal, which previous experiments have shown is roughly proportional to the square root of the product of ion density, electron density, and temperature:  $I_{LIF} = \sqrt{n_i n_e T_e}$ . The metastable state is pumped to the  $4p'^2 F_{7/2}^0$  state by a resonant vacuum wavelength of  $\lambda = 611.662$  nm. The upper state then decays to the  $4s'^2 D_{5/2}$  state with the emission of a photon at 461.086 nm. <sup>26</sup> The injected light is polarized parallel to the background magnetic field so that only the  $\pi$  transitions of the Zeeman split states are excited. The internal splitting of these  $\pi$  transitions is small and ignored in analysis. Stark broadening and natural and laser linewidth broadening are also negligible for these experimental conditions and are ignored in the analysis. 20,27 The laser power measured before the mechanical chopper (see Fig. 3) is  $\approx$ 1250 mW. The optical beam path has a total transmission of approximately 25% from the power measurement location to the output of the optical fiber, resulting in ≈320 mW of injected power. This power is well below the power broadening threshold of 470 mW reported in previous experiments for a comparable focal spot size and plasma density.<sup>22</sup>

The wavelength of a Sirah Matisse dye laser is swept  $\Delta f = \pm 8$  GHz around the transition wavelength of the initial metastable state over a 120 s scan time with a time constant of 1 s. 10% of the output of the laser is sampled by a Bristol 621 Wavemeter with an accuracy of  $\pm 0.0002$  nm. The absolute wavelength is determined with an iodine reference cell. The beam is mechanically chopped at 5 kHz and coupled into a 200  $\mu$ m core multimode optical fiber. Light carried through the fiber is then injected into the plasma through a  $\emptyset$  2 mm collimator in  $-\hat{x}$  and fluorescence is collected in  $+\hat{y}$  by optics with a spatial resolution of 1 mm. The collection optics couple light into a second 200  $\mu$ m multimode fiber, which is amplified by a Hamamatsu HC120–05MOD IR-sensitive photomultiplier tube (PMT). Background emission is rejected by a 1 nm bandpass filter centered at 461 nm. LIF signal is distinguished from spontaneous emission by a

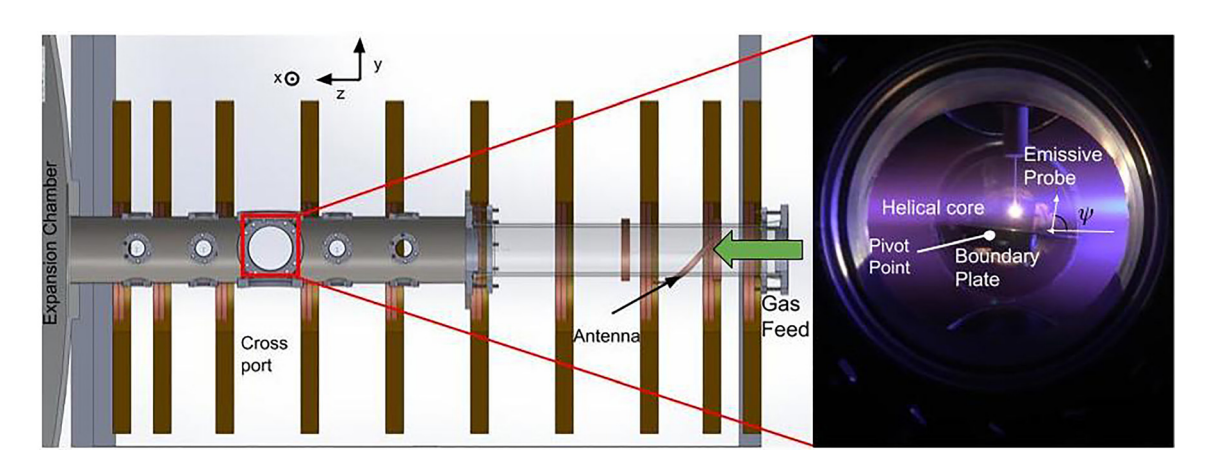


FIG. 2. Layout of the HELIX device for boundary measurement experiments. An expanded view of the boundary experiment domain is shown with the plate and probe immersed in the core of the plasma. The arrows show the direction of the background field and the plate normal.

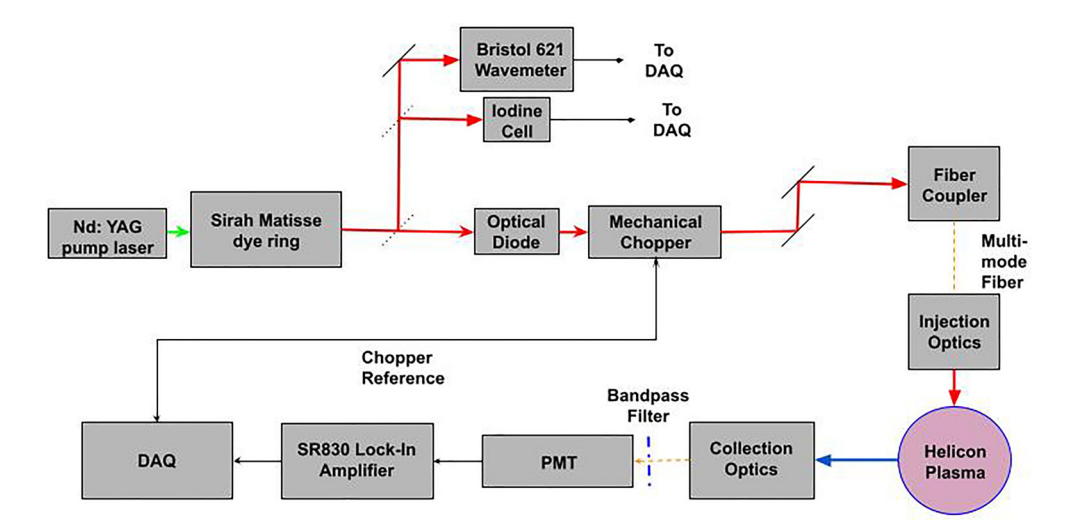


FIG. 3. Schematic of the injection and collection paths used for LIF measurements. Laser light is coupled into an optical fiber for transport to the plasma chamber and emission is coupled to a PMT. An iodine cell and a wavemeter provide real-time measurements of the laser wavelength.

Stanford Research Systems SR830 lock-in amplifier referenced to the chopper frequency. Figure 3 shows the injection and collection paths.

#### C. Langmuir probe

To measure the electron density,  $n_e$ , and electron temperature,  $T_e$ , a ø 0.5 × 2 mm² graphite tip Langmuir probe is inserted into the plasma. The probe is rf compensated at the half, first, and second harmonics of the antenna frequency. Simple Langmuir analysis techniques are problematic for magnetized rf plasmas. A probe will collect electrons along the magnetic field lines it intersects in addition to electrons transported across field lines to the probe surface. If the electron gyroradius of the system is close to the probe dimensions, given by  $\rho_e \sim r_p \ln l_p/r_p$  where  $r_p$  and  $l_p$  are probe radius and length, respectively, then current collection by the probe can be approximated by the Druyvesteyn method as detailed in previous work.

The Druyvesteyn method does not assume a particular distribution for the electrons when calculating  $n_e$  and  $T_e$ . This allows for accurate analysis despite non-Maxwellian features such as an energetic bump-on-tail or electron energy distribution functions not in thermal equilibrium. Measurements show that over a range of centimeters, the density only varied from  $2 \times 10^{17}$  to  $4.5 \times 10^{17}$  m<sup>-3</sup> across all angles of the boundary. The observed changes in  $T_e$  were less than the uncertainty in typical Langmuir probe measurement and the value is averaged to  $T_e \approx 5.1$  eV. The Langmuir probe uncertainty was determined from the standard deviation of data taken at a fiducial location, giving  $\delta n = 0.1 \times 10^{17}$  m<sup>-3</sup>,  $\delta T_e = 0.4$  eV, and  $\delta d = 0.7$  mm.

## D. Emissive probe

Measurements of the plasma potential above the disk are obtained with a  $\oslash 0.003 \times 2\,\mathrm{mm}^2$  tungsten filament emissive probe. The inflection point in the limit of zero emission method was used due to its minimization of space-charge effects. Potential measurements are achieved by measuring the inflection point of the I–V traces

as the probe's emission is varied close to the point of non-emission. From this value, a line is fit to the measured inflection points and extrapolated to the voltage at zero emission,  $I_{emiss}$ , which is the plasma potential. This analysis method benefits from small uncertainty, most of which is due to the fit.<sup>32</sup>

Sweeps of the emissive probe voltage are created by a triangular waveform generated by an Agilent 33220A Function Generator at 210 Hz with an applied DC offset. The signal was amplified by a custom-built circuit and applied to the filament. The resulting I–V traces were collected with a LeCroy Waverunner 604ZI oscilloscope and averaged over 1000 sweeps. The DC offset was applied to heat the filament, creating different values of  $I_{emiss}$ . The offset was varied from -600 to  $-1420\,\mathrm{mV}$  to obtain enough inflection points for a least squares linear fit.

#### III. RESULTS

Shown in Fig. 4 is the bulk ion flow in the  $\mathbf{E} \times \mathbf{B}$  direction as a function of normal distance from the boundary for a range of  $\psi$ . All flows are normalized to the ion sound speed,  $c_s \approx 3500$  m/s, based on the average electron temperature across the experimental domain. The IVDFs,  $T_e$ ,  $n_e$ , and  $V_p$  were measured from the surface of the plate to 8.6 gyroradii from the boundary. For some angles, the full range of distance was not accessible due to mechanical limitations. The distances from the boundary are normalized to the ion gyroradius,  $\rho_i = \sqrt{kT_im_i}/qB \sim 4.2$  mm. The ion mean free path,  $l \approx 11$  mm, is large compared to the Debye length  $(l \gg \lambda_D)$ , but comparable to  $\rho_i$ . This produces a mixed-collisional regime. The five different angles of the magnetic field are relative to the boundary normal,  $\psi = 83^\circ$ ,  $80^\circ$ ,  $75^\circ$ ,  $60^\circ$ , and  $45^\circ$  with an uncertainty of  $\delta\psi = \pm 1^\circ$ . For angles outside this range, the helicon core shifted to a new equilibrium far from the boundary.

The helical core equilibria were stable and highly reproducible as characterized by the uncertainty in the fiducial measurements. Uncertainty in the wavemeter measurements and shot-to-shot variations, determined from repeated measurements at a set of fiducial conditions, dominate the experimental error in the LIF measurements.

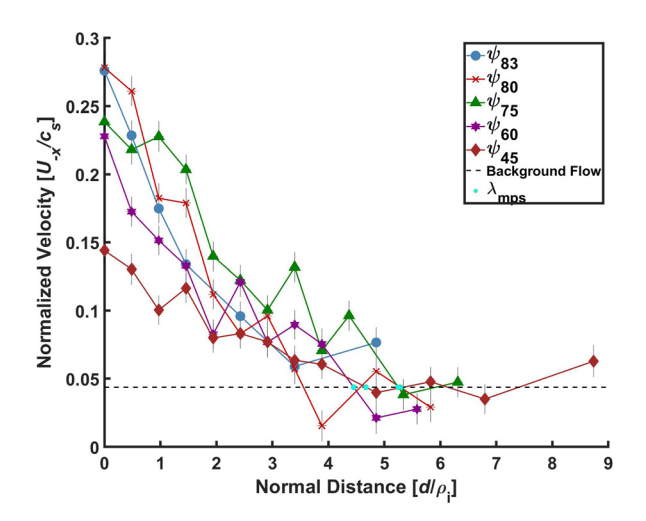


**FIG. 4.** Normalized ion velocity in the  $E\times B$  direction vs normalized distance above the boundary for all observed angles. The dashed line indicates the average background flow.

The velocity error is  $\sim 0.02c_s$ . Errors arising from uncertainty in the Gaussian fits of the IVDFs are negligible in comparison at a 95% confidence interval.

The flow measurements in the  $\mathbf{E} \times \mathbf{B}$  direction exhibit a trend of increasing speed with increasing  $\psi$ . The more oblique, i.e., perpendicular, the boundary is with respect to the magnetic field, the greater the ion drift near the boundary. By a distance of 3 gyroradii, the flows are within error of each other and all angles converge to the helicon background flow at  $\approx 0.04c_s$ . The background flow was determined by taking the velocity average in the  $\mathbf{E} \times \mathbf{B}$  direction for all measurement locations far from the plate  $(d/\rho_i > 5)$ . This ensures that the measurement locations are outside the effects of the magnetic presheath. Between 4.5 and 5.5 gyroradii, the  $\mathbf{E} \times \mathbf{B}$  flows converge to the background flow level and the distances at which that occurs are given in Table I. Note that the outlier velocity value for  $\psi = 80^{\circ}$  at  $d/\rho_i \approx 3.9$ was excluded in this analysis. Due to the mechanical limitations of the system, measurements were not possible far enough from the plate for  $\psi = 83^{\circ}$  for the measured flows to drop to the background flow. Table I gives estimates for where the edge of the magnetic presheath is located for each  $\psi$ .

**TABLE I.** The experimentally determined magnetic presheath lengths are based on when the velocity in the  $\mathbf{E} \times \mathbf{B}$  direction equals the background velocity. The measurements for  $\psi = 83^\circ$  were not taken far enough from the plate to observe the edge of the magnetic presheath,  $\lambda_{mps}$ . The magnetic presheath lengths for angles  $80^\circ$  and  $75^\circ$  are very close and well within error of each other, as are the values for angles  $60^\circ$  and  $45^\circ$ .

$\lambda_{mps}$	$d/ ho_i$
$\lambda_{83}$	>4.85
$\lambda_{80}$	≈5.29
$\lambda_{75}$	≈5.24
$\lambda_{60}$	≈4.45
$\lambda_{45}$	≈4.67

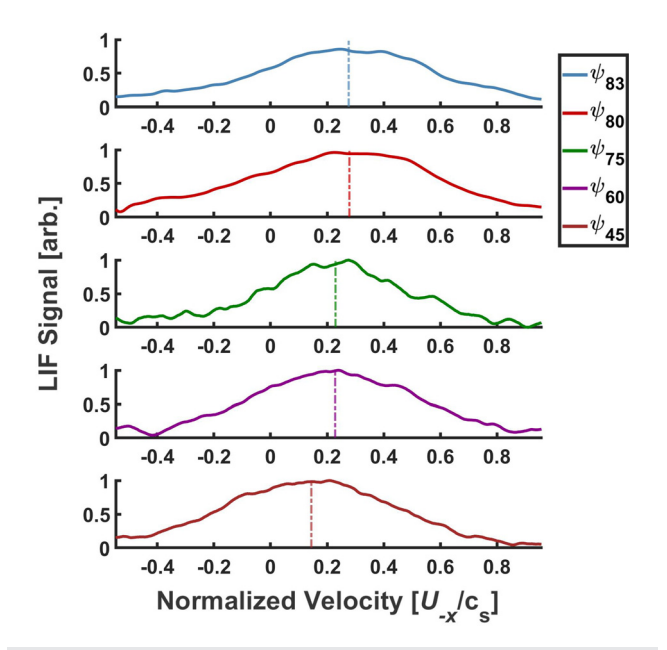


**FIG. 5.** IVDFs measured at the boundary for all  $\psi$  values. As the angle increases, the bulk ion flow in the  $\mathbf{E} \times \mathbf{B}$  direction increases. Vertical lines show the mean of the Gaussian fits.

The evolution of the IVDFs for all angles above the boundary is shown in Fig. 5. The bulk flows calculated from Gaussian fits to the measured distributions are shown with dashed lines and the x-axis is the velocity in the drift direction. As the angle between the boundary normal and the magnetic field increases, the bulk speed of the ions increases. Simply by rotating the boundary plate, the flow changes by as much as  $0.12c_s$ .

Shown in Fig. 6 are the ion flows for the measurement locations closest to the boundary  $(d/\rho_i = 0)$ , for all angles. A line of best fit

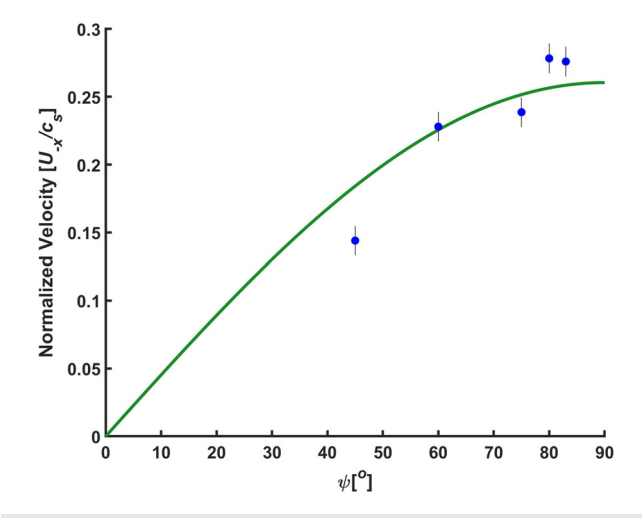


**FIG. 6.** Measured ion velocity taken at the boundary as a function of angle between the boundary normal and magnetic field. Experimental velocity data are shown as blue dots and the line of best fit is represented by the green line.

based on the residual sum of squares error was applied to these data in the form of

$$A \cdot \sin(\psi),$$
 (5)

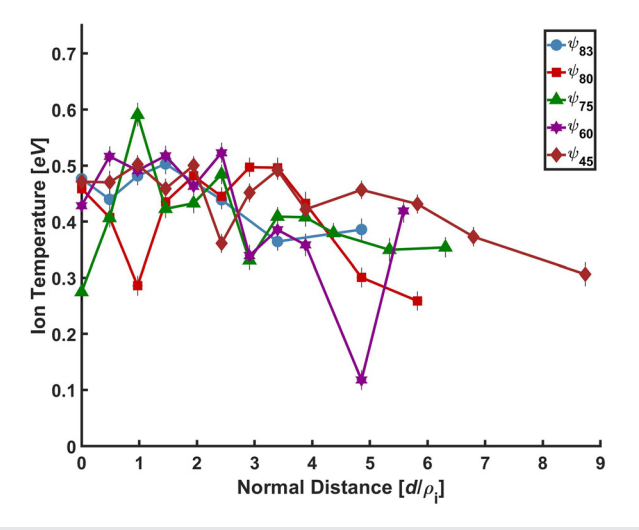
where A is a fitting parameter equal to  $0.26c_s$ . From Eq. (3), the parameter A is equivalent to the ratio of  $\frac{E}{B}$ . Since the strength of the magnetic field is known, 0.1 T, the fit to the flows provides an average magnitude of the electric field, E=95 V/m, that is directed into the plate. This analysis, however, assumes that  $\psi$  has a negligible influence on the structure and magnitude of the electric field in the presheath.

The ion temperatures as a function of normalized distance from the boundary for all angles between the boundary normal and the magnetic field are shown in Fig. 7. For all angles, the ion temperature decreases slightly with increasing normalized distance. There appears to be no consistent trend of ion temperature with  $\psi$ . The error in  $T_i$  values is determined by the shot-to-shot variations in the fiducial measurements and has a value of  $\delta T_i = 0.04$  eV. The average ion temperature in Fig. 7 is  $T_i = 0.43$  eV, which is typical of Ar II temperatures measured in HELIX. <sup>21,33</sup>

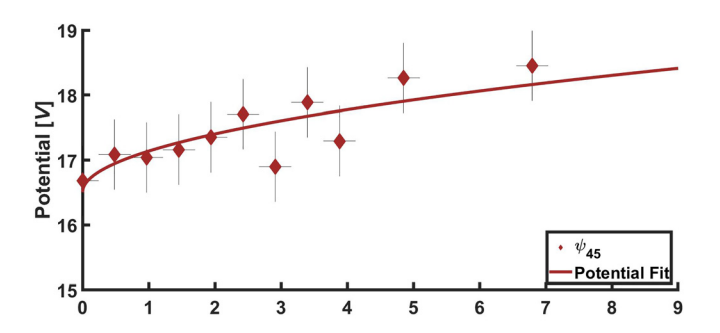
Figure 8 shows the plasma potential as a function of normalized distance from the boundary for all angles of the boundary normal relative to the magnetic field. Consistent with previous emissive probe measurements in other systems, <sup>34,35</sup> there is a sharp increase in the potential near the electrostatic sheath and followed by a more gradual increase throughout the magnetic presheath. A function of the form

$$V_p = \frac{T_e}{e} \sqrt{\frac{(d - d_0)}{l}} + V_o,$$
 (6)

where l is the ion-neutral collision length,  $d_0$  is the location of the boundary, and  $V_o$  is the potential at zero distance,<sup>34</sup> was fit to the measurements. The presheath electric field was then determined analytically from the potential fit using  $E_{calc} = \frac{\Delta V}{\Delta d}$ . Emissive probes are able to resolve difference in potential as small as 0.2 V;<sup>36</sup> however, our measurements had a shot-to-shot variation of  $\delta V_p = 0.3$  V. An example



**FIG. 7.** Ion temperature vs normalized distance for different values of the  $\psi$  relative to the boundary normal.



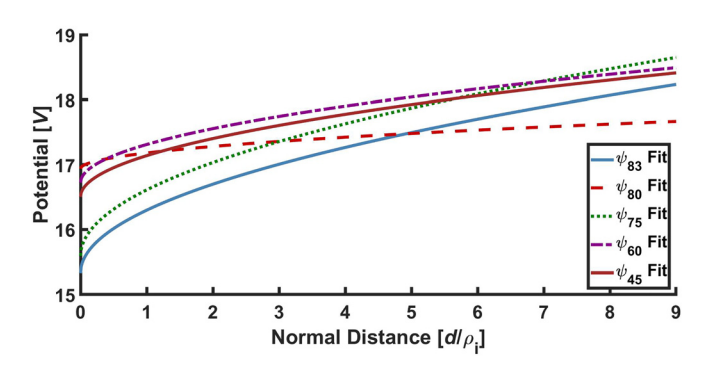


**FIG. 8.** Plasma potential from emissive probe measurements as a function of normalized distance from the boundary for all the observed  $\psi$ . (a) Sample of the data and the corresponding fit. (b) Fits for all angles.

of the emissive probe measurements and a fit are shown in Fig. 8(a) for  $\psi=45^\circ$ . The fits obtained from measurements at other  $\psi$  values are shown in Fig. 8(b). Because there is considerable scatter in the measured potentials, all of the raw measured values are not shown in Fig. 8(b). However, the fit errors arising from scatter in the potential measurements are reflected in the calculated flows of Fig. 9.

The electric fields obtained from the analytic derivative of Eq. (6) were used with Eq. (3) to predict the expected values for the  $v_{E\times B}$ drifts. Uncertainties in the measured potentials result in uncertainties in the electric field of up to  $\delta E_{calc} = 34\%$ . Shown in Fig. 9 is a comparison of the predicted flows with the measured flows for all  $\psi$  values out to a distance 2.4 gyroradii from the boundary. In all but one case, the measured flows are smaller than the predicted values. The measured flows (red) for  $\psi=60^\circ$  and  $\psi=45^\circ$  are in good agreement with the predicted values (black) in both magnitude and scaling with distance from the boundary. The measured flows for  $\psi = 83^{\circ}$  and  $\psi = 75^{\circ}$  exhibit the same scaling with distance as the predicted values, but the absolute magnitudes of the flows lie outside of the error range of the predictions. The measured flows for  $\psi = 80^{\circ}$  are the only case in which the measured values are larger than the predictions. The scaling with distance is consistent between the measured and predicted flow values, but the magnitudes of the measurements lie outside of the range of the errors in the predicted values. We note that the emissive probe measurements for  $\psi = 80^{\circ}$  were particularly noisy and the resultant fit probably underestimate the electric field in the presheath by a large amount. In all cases, the calculated flows nearest to the boundary are suspect because the rapidly changing potentials near the

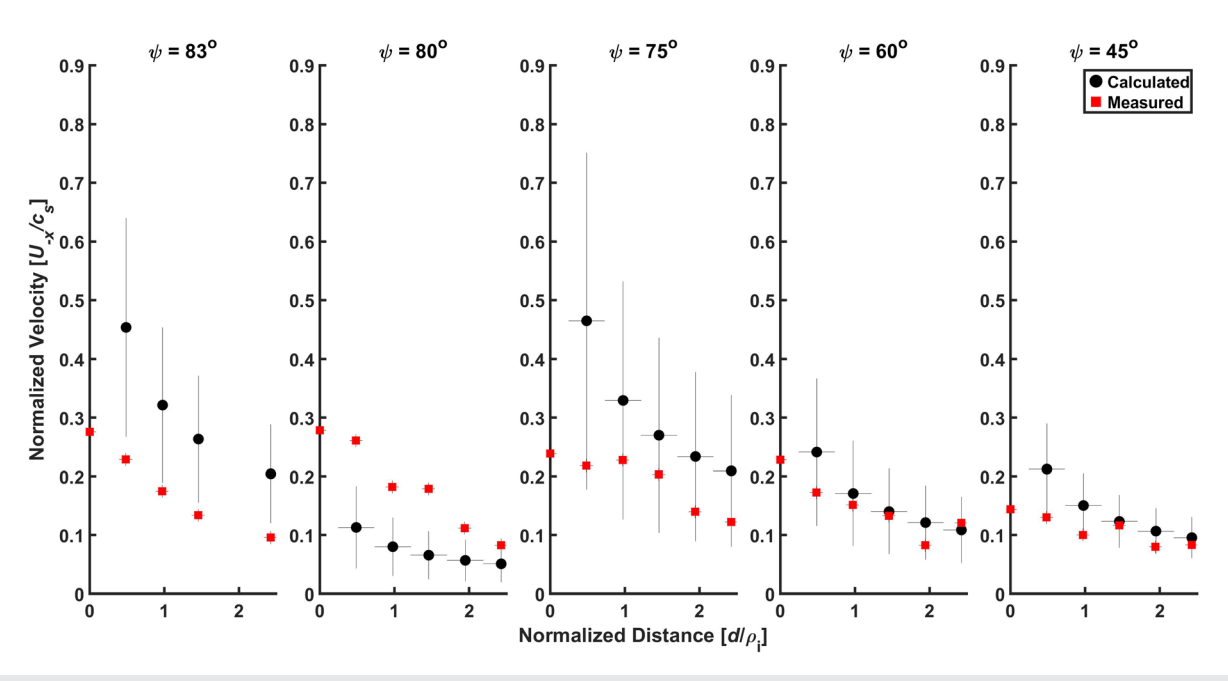


**FIG. 9.** Comparison of the  $\mathbf{E} \times \mathbf{B}$  flows predicted from  $E_{calc}$  calculations (black circles) with the experimentally measured flows (red squares). The high speed calculated flows at the boundary are artifacts due to poor fits to the measured potentials.

boundary introduce significant uncertainty into the electric field estimations.

#### IV. DISCUSSION

For all values of  $\psi$  investigated, there is a clear decrease in ion flow speed in the  $\mathbf{E} \times \mathbf{B}$  direction with increasing distance from the boundary. A previous study found the maximum ion flow speed in the  $\mathbf{E} \times \mathbf{B}$  direction occurred at half a gyroradius from the boundary surface. However, here we find that the maximum ion flow occurs at the closest point of measurement to the boundary surface. This is actually the expected location for maximum  $\mathbf{E} \times \mathbf{B}$  flow, since the bulk of the potential drop occurs in the electrostatic sheath and the "transition region."  $^{34-36}$ 

Our measurements agree with previous work in that the edge of the magnetic presheath is much closer to the boundary than Chodura predicted. <sup>19,20</sup> Using Eq. (1) as an estimate, the boundary of the magnetic presheath for our plasma parameters is predicted to occur at a distance of 7.6 gyroradii from the boundary for an angle of  $\psi = 60^{\circ}$ . However, according to Table I, we see that the ions do not feel a force in the E × B direction until ~5.3 gyroradii or closer. Therefore, the potential in the magnetic presheath drops to a negligible level much closer to the plate than predicted. This LIF technique provides an indirect method of experimentally measuring  $\lambda_{mps}$  by determining the location at which  $v_{E\times B} = 0$ . One possible cause of this reduced electric field may be from the difference in ion and electron gyroradii. <sup>37</sup> In this case, at high  $\psi$  values, the large gyro-orbits of the ions will shift the ratio of particle flux to the boundary such that the potential drop across the sheath is reduced.

Fitting the  $v_{E\times B}$  at the edge of the sheath with Eq. (5) provides a qualitative method for determining the average electric field at the boundary of the electrostatic sheath. The sine fit gives an average electric field of -95 V/m. However, the calculated electric field from the

experimentally measured potential profiles is two to three times larger close to the boundary surface. Since we were unable to accurately describe the electric field at d=0, the angular dependence of the magnetic sheath electric field is not fully understood. The observed changes in ion flow with  $\psi$  (Fig. 9) likely result from a combination of the change in the projection of the electric field along the magnetic field and overall changes in the potential across the sheath that arise from changes in the  $\psi$ .

LIF bulk flow measurements of the  $v_{E\times B}$  drift show promise as a non-perturbative method to measure electric field structure in the magnetic presheath. This method would allow for the electric potential of magnetized plasmas to be obtained without disturbing the sheath structure and without concerns for probe survivability or plasma contamination. Provided optical access exists, this method can provide E-field measurements in a variety of plasma-boundary systems, such as the highly oblique magnetic field case similar to the conditions at divertor. Conditions in HELIX cannot match those in a tokamak scrape-off layer (SOL), but experimental investigations of this region can provide many insights into the kinetic effects present at oblique magnetic fields.

#### **ACKNOWLEDGMENTS**

The authors would like to thank Thomas Steinberger for his helpful insights and analytic expertise. This work is supported by U.S. National Science Foundation (NSF) Award Nos. PHYS 1827325 and 1902111 and DoE Award No. DE-SC0020294.

# DATA AVAILABILITY

The data that support the findings of this study are available from the corresponding author upon reasonable request.

#### REFERENCES

- <sup>1</sup>R. Chodura, "Plasma-wall transition in an oblique magnetic field," Phys. Fluids **25**, 1628–1633 (1982).
- <sup>2</sup>I. Y. Senichenkov, E. Kaveeva, E. Sytova, V. Rozhansky, S. Voskoboynikov, I. Y. Veselova, D. Coster, X. Bonnin, and F. Reimold, "On mechanisms of impurity leakage and retention in the tokamak divertor," Plasma Phys. Controlled Fusion 61, 045013 (2019).
- <sup>3</sup>P. Stangeby and A. Chankin, "The ion velocity (Bohm–Chodura) boundary condition at the entrance to the magnetic presheath in the presence of diamagnetic and E × B drifts in the scrape-off layer," Phys. Plasmas 2, 707–715 (1995).
- <sup>4</sup>P. Stangeby and A. Chankin, "Simple models for the radial and poloidal E × B drifts in the scrape-off layer of a divertor tokamak: Effects on in/out asymmetries," Nucl. Fusion 36, 839 (1996).
- <sup>5</sup>J. Loizu, P. Ricci, F. Halpern, and S. Jolliet, "Boundary conditions for plasma fluid models at the magnetic presheath entrance," Phys. Plasmas 19, 122307 (2012).
- <sup>6</sup>J. Loizu, J. Morales, F. Halpern, P. Ricci, and P. Paruta, "Scrape-off-layer current loops and floating potential in limited tokamak plasmas," J. Plasma Phys. 83, 575830601 (2017).
- <sup>7</sup>D. Tskhakaya, "One-dimensional plasma sheath model in front of the divertor plates," Plasma Phys. Controlled Fusion 59, 114001 (2017).
   <sup>8</sup>L. Popova, G. Kamberov, T. Nikolov, P. Marinov, and D. Mitev, "Method for
- <sup>8</sup>L. Popova, G. Kamberov, T. Nikolov, P. Marinov, and D. Mitev, "Method for simulation of particle recombination in SOL plasma," Bulg. J. Phys 32, 263–271 (2005).
- <sup>9</sup>A. Geraldini, F. I. Parra, and F. Militello, "Gyrokinetic treatment of a grazing angle magnetic presheath," Plasma Phys. Controlled Fusion 59, 025015 (2017).
- <sup>10</sup> F. D. Halpern, P. Ricci, S. Jolliet, J. Loizu, J. Morales, A. Mosetto, F. Musil, F. Riva, T.-M. Tran, and C. Wersal, "The GBS code for tokamak scrape-off layer simulations," J. Comput. Phys. 315, 388–408 (2016).
- <sup>11</sup>K.-U. Riemann, "Theory of the collisional presheath in an oblique magnetic field," Phys. Plasmas 1, 552–558 (1994).
- <sup>12</sup>E. Ahedo and D. Carralero, "Model of a source-driven plasma interacting with a wall in an oblique magnetic field," Phys. Plasmas 16, 043506 (2009).
- <sup>13</sup>K.-U. Riemann, "The Bohm criterion and sheath formation," J. Phys. D 24, 493 (1991).
- <sup>14</sup>S.-B. Wang and A. E. Wendt, "Sheath thickness evaluation for collisionless or weakly collisional bounded plasmas," IEEE Trans. Plasma Sci. 27, 1358–1365 (1999).
- 15E. Ahedo, "Structure of the plasma-wall interaction in an oblique magnetic field," Phys. Plasmas 4, 4419–4430 (1997).
- <sup>16</sup>P. Stangeby, "The Bohm-Chodura plasma sheath criterion," Phys. Plasmas 2, 702-706 (1995).
- <sup>17</sup>P. Stangeby, "The Chodura sheath for angles of a few degrees between the magnetic field and the surface of divertor targets and limiters," Nucl. Fusion 52, 083012 (2012).
- <sup>18</sup>M. U. Siddiqui, C. D. Jackson, J. F. Kim, and N. Hershkowitz, "Direct measurements of ion dynamics in collisional magnetic presheaths," Phys. Plasmas 21, 102103 (2014).
- <sup>19</sup>M. U. Siddiqui, D. S. Thompson, C. D. Jackson, J. F. Kim, N. Hershkowitz, and E. E. Scime, "Models, assumptions, and experimental tests of flows near boundaries in magnetized plasmas," Phys. Plasmas 23, 057101 (2016).

- <sup>20</sup>D. S. Thompson, R. Khaziev, M. Fortney-Henriquez, S. Keniley, E. E. Scime, and D. Curreli, "Three-dimensional cross-field flows at the plasma-material interface in an oblique magnetic field," Phys. Plasmas 27, 073511 (2020).
- <sup>21</sup>E. E. Scime, P. A. Keiter, M. M. Balkey, J. L. Kline, X. Sun, A. M. Keesee, R. A. Hardin, I. A. Biloiu, S. Houshmandyar, S. C. Thakur, J. Carr, M. Galante, D. McCarren, and S. Sears, "The hot helicon experiment (HELIX) and the large experiment on instabilities and anisotropy (LEIA)," J. Plasma Phys. 81, 345810103 (2015).
- <sup>22</sup>E. Scime, R. Hardin, C. Biloiu, A. Keesee, and X. Sun, "Flow, flow shear, and related profiles in helicon plasmas," Phys. Plasmas 14, 043505 (2007).
- <sup>23</sup>F. Chu, R. Hood, and F. Skiff, "Measurement of wave-particle interaction and metastable lifetime using laser-induced fluorescence," Phys. Plasmas 26, 042111 (2019).
- <sup>24</sup>Y.-K. Lee and C.-W. Chung, "Ionization in inductively coupled argon plasmas studied by optical emission spectroscopy," J. Appl. Phys. 109, 013306 (2011).
- <sup>25</sup>X. Sun, C. Biloiu, R. Hardin, and E. E. Scime, "Parallel velocity and temperature of argon ions in an expanding, helicon source driven plasma," Plasma Sources Sci. Technol. 13, 359 (2004).
- <sup>26</sup>G. Severn, D. Edrich, and R. McWilliams, "Argon ion laser-induced fluorescence with diode lasers," Rev. Sci. Instrum. 69, 10–15 (1998).
- <sup>27</sup>R. Bovin, "Study of the different line broadening mechanisms for the laser induced fluorescence diagnostic of the HELIX and LEIA plasmas," Technical Report No. PL-039 (West Virginia University, 1998).
- <sup>28</sup>R. Boivin, "Study of the different line broadening mechanisms for the laser induced fluorescence diagnostic of the HELIX and LEIA plasmas," Technical Report No. PL-039 (West Virginia University Plasma Physics Lab, Morgantown, WV, 2000).
- <sup>29</sup>V. Demidov, S. V. Ratynskaia, and K. Rypdal, "Electric probes for plasmas: The link between theory and instrument," Rev. Sci. Instrum. 73, 3409–3439 (2002).
- <sup>30</sup>V. Godyak and V. Demidov, "Probe measurements of electron-energy distributions in plasmas: What can we measure and how can we achieve reliable results?," J. Phys. D 44, 233001 (2011).
- <sup>31</sup>J. Sheehan and N. Hershkowitz, "Emissive probes," Plasma Sources Sci. Technol. 20, 063001 (2011).
- <sup>32</sup>J. Sheehan, Y. Raitses, N. Hershkowitz, I. Kaganovich, and N. J. Fisch, "A comparison of emissive probe techniques for electric potential measurements in a complex plasma," Phys. Plasmas 18, 073501 (2011).
- <sup>33</sup>J. Kline, E. Scime, R. Boivin, A. Keesee, X. Sun, and V. Mikhailenko, "RF absorption and ion heating in helicon sources," Phys. Rev. Lett. 88, 195002 (2002).
- 34L. Oksuz and N. Hershkowitz, "Plasma, presheath, collisional sheath and collisionless sheath potential profiles in weakly ionized, weakly collisional plasma," Plasma Sources Sci. Technol. 14, 201 (2005).
- 35B. Singha, A. Sarma, and J. Chutia, "Experimental observation of sheath and magnetic presheath over an oblique metallic plate in the presence of a magnetic field," Phys. Plasmas 9, 683–690 (2002).
- <sup>36</sup>L. Oksuz and N. Hershkowitz, "First experimental measurements of the plasma potential throughout the presheath and sheath at a boundary in a weakly collisional plasma," Phys. Rev. Lett. 89, 145001 (2002).
- <sup>37</sup>N. S. Krasheninnikova, X. Tang, and V. S. Roytershteyn, "Scaling of the plasma sheath in a magnetic field parallel to the wall," Phys. Plasmas 17, 057103 (2010).